

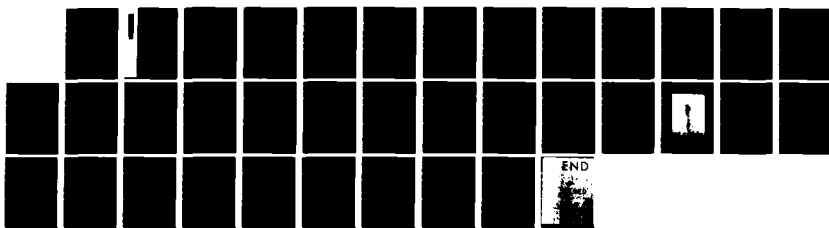
RD-A127 018 EXTRATION AND PROPAGATION OF AN INTENSE ROTATING  
ELECTRON BEAM(U) MISSION RESEARCH CORP ALBUQUERQUE NM  
R J ADLER ET AL. OCT 82 AMRC-R-422 SNL-16-5234

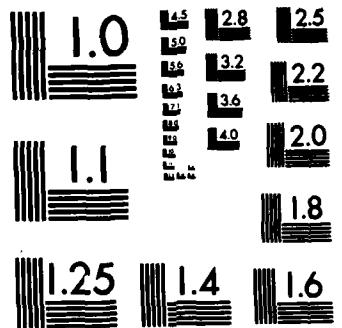
1/1

UNCLASSIFIED

.F/G 28/7

NL





AMRC-R-422  
October 1982  
Copy *1*

EXTRACTION AND PROPAGATION OF AN INTENSE,  
ROTATING ELECTRON BEAM

R. J. Adler  
G. F. Kiuttu  
T. P. Hughes  
Mission Research Corporation

and

B. Sabol  
Air Force Weapons Laboratory  
Kirtland Air Force Base, New Mexico 87117

Prepared for:

Sandia National Laboratories  
Pulse Power Directorate  
Albuquerque, New Mexico 87185

and

Air Force Weapons Laboratory  
Kirtland Air Force Base  
New Mexico 87117

Under Contract:

SNL 16-5234

DTIC

APR 20 1983

A

Prepared by:

MISSION RESEARCH CORPORATION  
1720 Randolph Road, S.E.  
Albuquerque, New Mexico 87106

Approved for public release and sale, no  
restrictions apply.

83 02 020 069

DTIC FILE COPY

## TABLE OF CONTENTS

<u>Section</u>	<u>Page</u>
ABSTRACT	iii
I. INTRODUCTION	1
II. EQUILIBRIUM PROPERTIES	3
III. EXPERIMENTAL RESULTS	5
IV. NUMERICAL SIMULATIONS OF EXTRACTION AND FILAMENTATION	25
REFERENCES	31

Accession For	
NTIS GRA&I	
DTIC TAB	
Unannounced	
Justification	
<i>Not on file</i>	
By	
Distribution/	
Availability Codes	
Avail and/or	
DIST	Special
A	



## LIST OF ILLUSTRATIONS

<u>Figure</u>	<u>Page</u>
1a Experimental setup.	6
1b Axial magnetic profile with and without half-cusp plate.	7
2 Microdensitometer scan of a blue cellophane witness foil positioned at the anode. Change in percent transmission is proportional to time averaged current density.	8
3 Beam radius measured from radiochromic witness foils as a function of cathode magnetic field. Experimental conditions are $P = .25$ Torr, $I_{net} = 11$ kA, with the plate in. Measurements were made at $z = 10$ cm.	10
4 Energy propagation inside an $r = 2.5$ cm aperture with and without applied diode magnetic field. Measurements were made at a 30 cm axial position.	11
5 Ratio of injected energy ( $R < 2.5$ cm) to injected diode energy vs. pressure for 3.7 kG, $z = 60$ cm, and a $4^\circ$ scattering angle.	13
6 Ratio of net to current diode for $4^\circ$ scattering and a variety of cathode magnetic fields.	14
7 Isodensity contour plots showing two radiochromic foils positioned at $z = 25$ cm. The equal transmission density contours are ranked in linear order of increasing exposure (increasing current density). (a) .3 Torr, (b) 20 Torr.	16
8 Beam rotation velocities as a function of radius for various cathode magnetic fields. Dashed lines are taken from Eq. (1).	19
9 Raw emittance box data illustrating the typical angled pattern for $B_z = 1$ kG.	20
10 Comparison of $B_z$ and $B_\theta$ waveforms for a) $z = 18$ , $P = .3$ , $B_z = 1.8$ ; b) $z = 18$ , $P = 20$ , $B_z = 1.8$ ; c) $z = 43$ , $P = 20$ , $B_z = 1.8$ ; d) $z = 68$ , $P = 20$ , $B_z = 2.6$ . Relative $B_z$ units.	22
11 The plot above indicates curves of $\omega_c$ and $v_c$ (collision frequency) in the peak beam magnetic field where $v_c$ is the momentum transfer collision frequency and $\omega_c$ is the plasma electron cyclotron frequency.	24
12 Simulations for $B_z = 1$ kG, 2 kG, and 4 kG. For each value the radial positions of the beam particles are plotted versus axial position. The radial coordinate is in logarithmic units.	26

## ABSTRACT

A hollow electron beam produced in a strong axial magnetic field has been extracted into a neutral gas cell where the magnetic field is zero. Due to radial magnetic field in the transition region, the beam rotates and maintains its hollow profile. Equilibrium is provided by the  $v_z \times B_\theta$  inward force and centrifugal outward force. We have studied both extraction and propagation phenomena in this configuration. Measurements include beam and net currents, beam generated axial magnetic fields, beam rotation and emittance, and light produced. A filamentation instability has been observed outside the magnetic field in this configuration. Beam equilibrium results are also presented and are compared with both experiment and numerical simulation.

## I. INTRODUCTION

Both intense electron beam propagation in neutral gas,<sup>1-5</sup> and the interaction of rotating electron beams with plasma<sup>6-10</sup> are subjects of significant interest. Neutral gas propagation has been studied in connection with such areas as plasma heating,<sup>7</sup> collective ion acceleration,<sup>1</sup> and laser pumping. Rotating beam production is important in areas such as plasma confinement,<sup>9</sup> electron ring acceleration, accelerator transport,<sup>11,12</sup> and betatron acceleration.<sup>13</sup>

In this work, we discuss results on the case of a rotating propagating beam. Previous work on rotating beams in initially neutral gas or plasma typically treats the case where an applied magnetic field provides beam confinement. Experiments on beam propagation outside a magnetic field have been performed in the absence of rotation, with one exception.<sup>9</sup> Sethian et. al. have studied the case of a rotating beam of low average axial velocity confined by its self-generated  $B_z$  field.

In this work we study the propagation of a rotating beam confined by its  $B_\theta$  (pinch) field. In the rotating beam propagation mode studied, both the beam radius and rotation velocity can be controlled by changing the magnetic field at the cathode. Beam propagation is found to differ from the case of a nonrotating beam due to the filamentation instability observed in the hollow beam, the reduced manifestation of the resistive hose instability, and the increased beam diameter.

Our measurements deal with the rotating nature of the beam directly through emittance box data, and beam-generated axial magnetic field data. In addition, the usual propagation parameters such as net current and energy transport have been studied. Numerical work includes simulation of the half-cusp region and subsequent radial oscillations.

In Section II we outline the simple theoretical considerations which define the beam equilibrium. Section III summarizes the results from experiments on the VISHNU accelerator. In Section IV, numerical work relating to the extraction problem is presented.

## II. EQUILIBRIUM PROPERTIES

The dominant feature of the beam equilibrium in gas is the balance between the outward  $P_\theta$  force, and the inward pinch force due to the net axial current  $I$ . We treat an infinitessimally thin hollow beam produced on a cathode of radius  $r_c$  in a region of axial magnetic field  $B_c$ . Conservation of canonical angular momentum between the source region and the zero-field region gives the azimuthal particle velocity for a particle at radius 'a' as

$$v_\theta = \frac{\omega_c r_c^2}{2a} \quad (1)$$

where  $\omega_c = eB_c/\gamma mc$ ,  $\gamma$  is the beam relativistic factor, we assume  $v_z \sim c$ , and other symbols have their usual meanings. The pinch force is zero on the inside of the beam in gas, and has the value  $2eI/ac$  on the outside so we take the pinch force averaged over a particle orbit as  $eI/ac$ . Note that in the type of equilibrium we discuss, laminar flow is not possible. No pinch force is applied to the inner electrons so they move outward due to centrifugal force. Outer electrons must be turned inward by the pinch force, or equilibrium is lost.

The force balance condition is then

$$\frac{\gamma mv_\theta^2}{a} = \frac{eI}{ac} \quad (2)$$

Combining (1) and (2), we find the cold beam equilibrium radius to be

$$\frac{a}{r_c} = \frac{r_c \omega_c}{2c} \left( \frac{I_A}{T} \right)^{1/2} \quad (3)$$

where  $I_A = \gamma mc^3/e$  is the usual Alfvén current. Note that this equilibrium is distinguished from previous rotating beam experiments because  $v_z \times B_\theta$  provides the electron confinement force. The basic dependence of the beam radius in (3) is rather curious -  $a \propto \phi/(\gamma I)^{1/2}$  where  $\phi$  is the magnetic flux encircled by the cathode  $\phi = \pi r_c^2 B_c$ .

Linearizing the equation of motion around the equilibrium, we can find the wavelength of small radial oscillations as

$$\lambda = \pi a \left( \frac{I_A}{I} \right)^{1/2} = \frac{\pi r_c^2 \omega_c}{2c} \left( \frac{I_A}{I} \right) \quad (4)$$

The radial and azimuthal perturbations are related by

$$\frac{a \delta \dot{\theta}}{c} = -2 \left( \frac{I}{I_A} \right) \frac{\delta a}{a} \quad (5)$$

The numerical work of Section IV indicates that radial oscillations result from pinching at the extraction foil,<sup>14</sup> mismatches in radius before and after the foil, and the non-laminar type of flow.

### III. EXPERIMENTAL RESULTS

The experimental setup used to study rotating beam propagation is shown in Fig. 1a. The beam is produced in a vacuum diode from a 3.35 cm OD, 2.7 cm ID annular cathode spaced nominally 2.0 cm from the foil anode. A quasi-DC ( $\sim 200$  msec) magnetic field was produced by an outer solenoid, a mild steel cathode shank, and an optional cusp plate. The measured magnetic field profile is shown in Fig. 1b. Magnetic field values at the cathode varied from 0-4 kG so that the average beam magnetic flux was  $0-2.8 \times 10^{-4}$  Webers. The peak diode voltage was typically .9-1.0 MV, with peak diode currents from 15-25 kA.

A number of diagnostics are indicated in Figure 1. Both net current and beam current were measured using magnetic pick-up loop arrays at various positions. Energy transport over 25, 50, and 75 cm distances was measured using a carbon calorimeter. The time-averaged beam rotation and emittance were measured using an array of 750  $\mu\text{m}$  holes in 375  $\mu\text{m}$  thick Tantalum foil as an emittance mask. A photograph of a piece of scintillating plastic was used to register the emittance box projections. Beam-generated  $B_z$  was monitored using an axis-encircling loop in a cage (the cage allowed return of z-currents, but not  $\theta$ -currents. Diode voltage and current were measured on every shot. Radiochromic witness foils which are sensitive only to high energy particles<sup>15</sup> were used to measure beam radius.

The beam profile at several axial positions was observed with radiochromic witness foils. A microdensitometer scan of the beam at the anode foil is shown in Fig. 2. Numerical integration of the data, under the assumption that current density is proportional to change in transmission, indicates that less than 10% of the current is found at  $r < 1.2$  cm. The

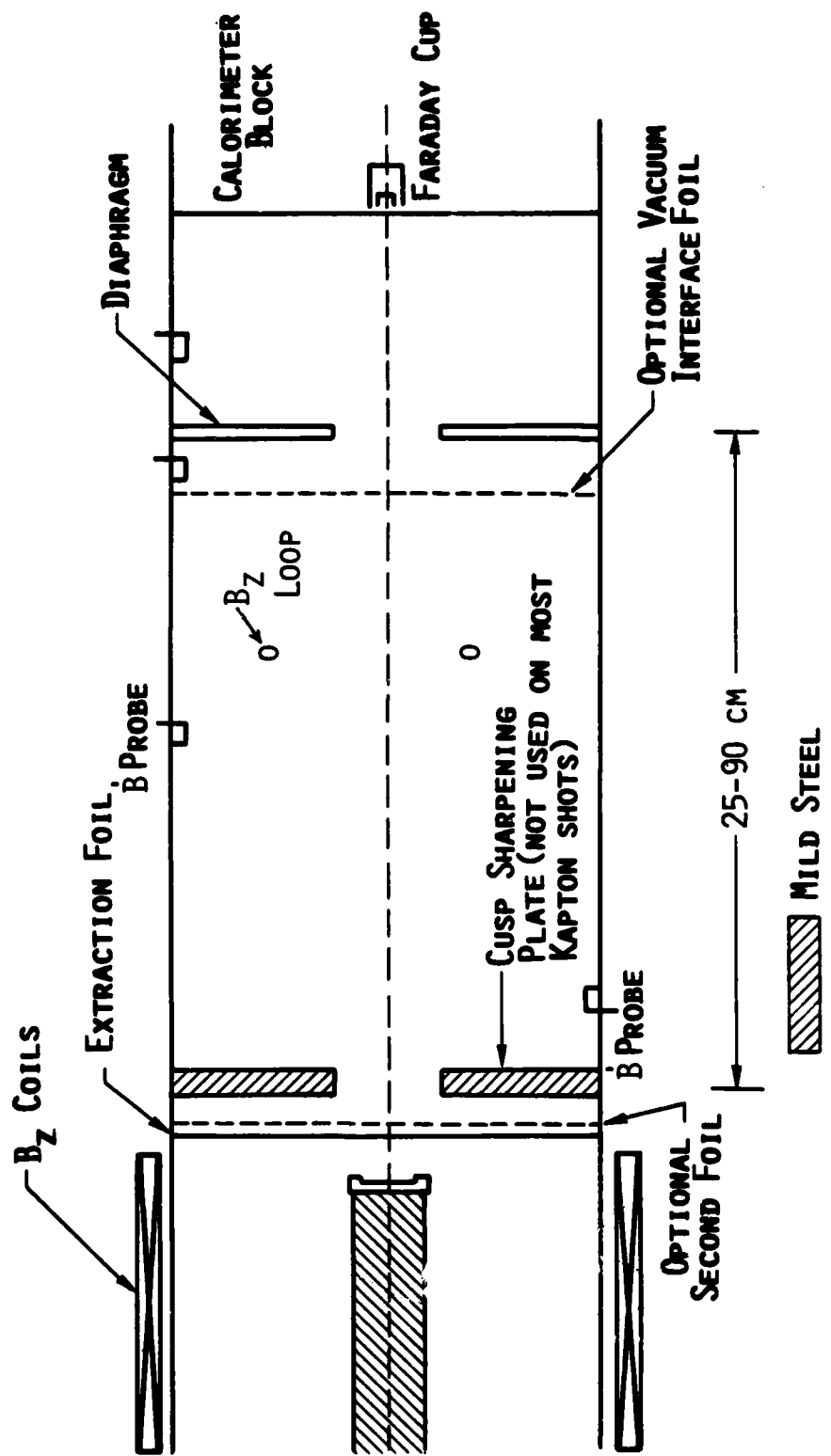


Figure 1a. Experimental Setup.

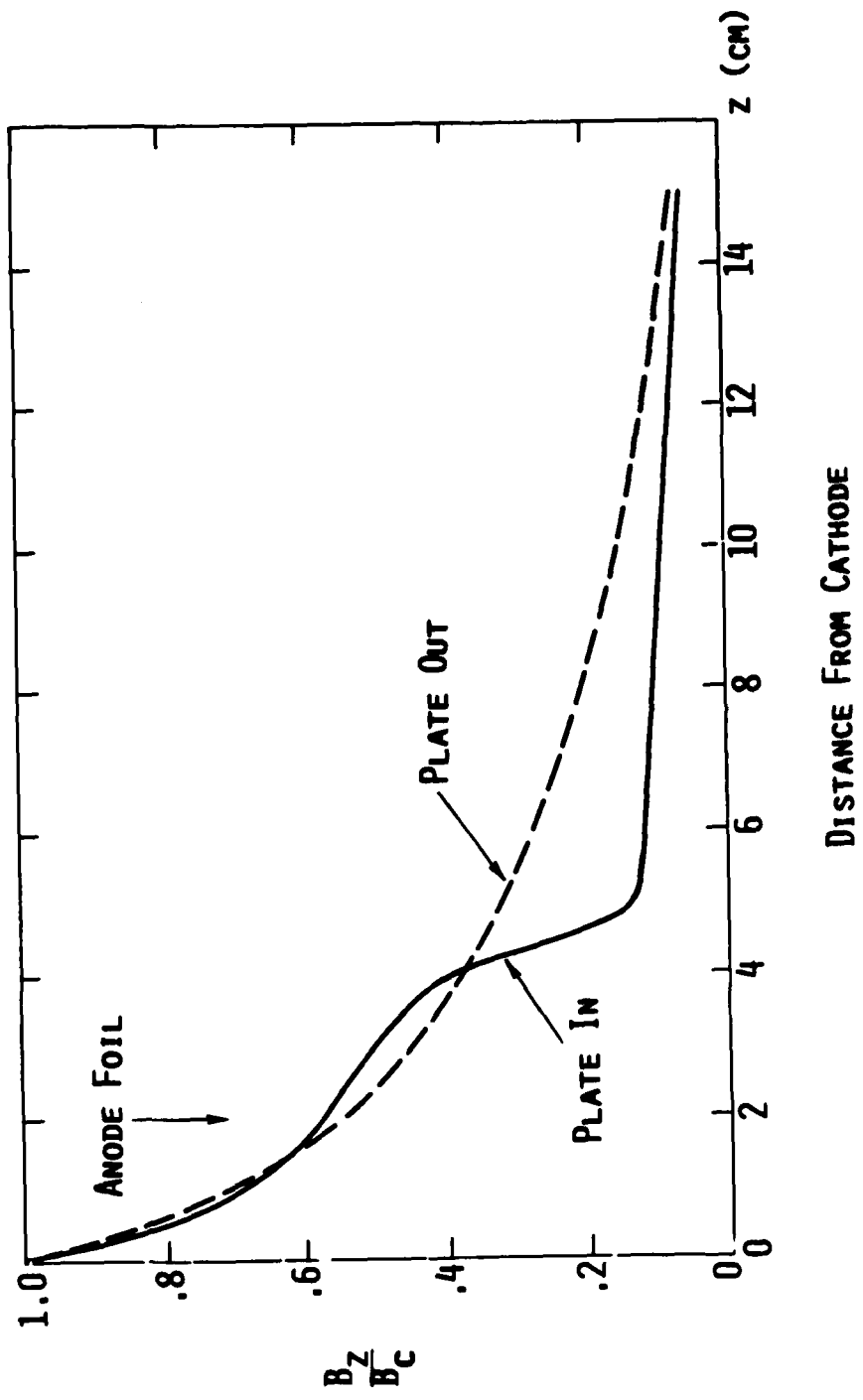


Figure 1b. Axial magnetic profile with and without half-cusp plate.

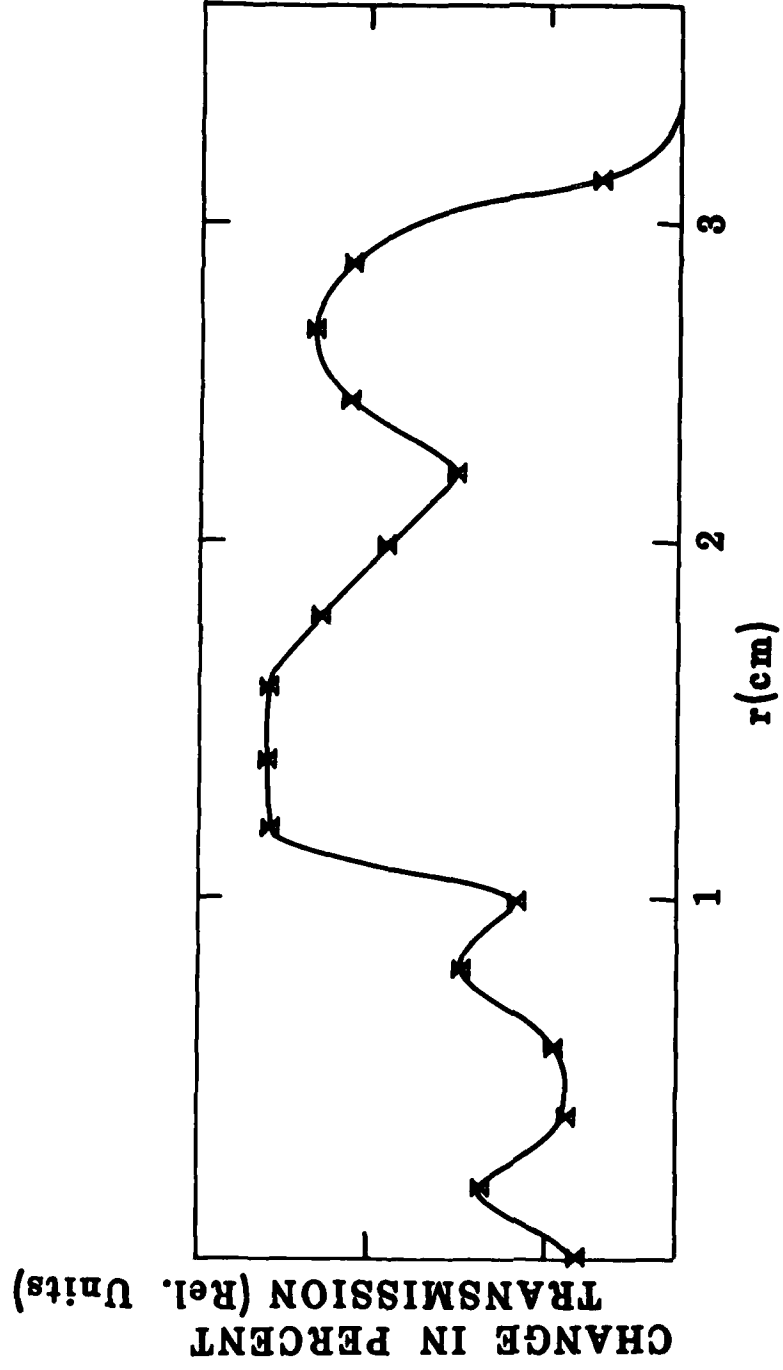
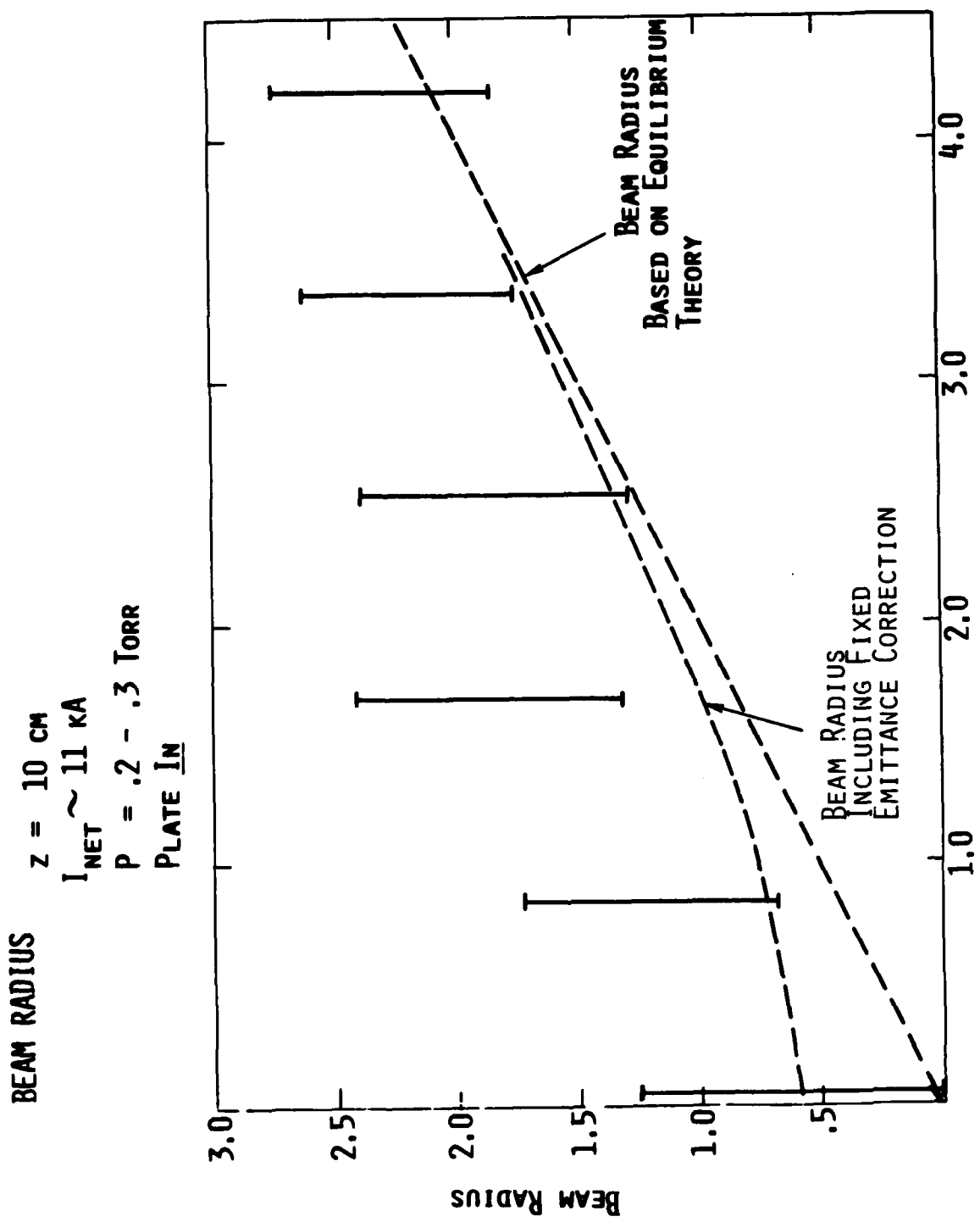


Figure 2. Microdensitometer scan of a blue cellophane witness foil positioned at the anode. Change in percent transmission is proportional to time averaged current density.

outer radius is much larger than the 1.7 cm cathode radius. This is probably due to particles emitted radially from behind the cathode face. Significant emission from this region is expected to raise the average  $P_\theta$  of the beam. The dosimeter scan of Fig. 2 typifies  $B \neq 0$  shots, however, diode pinching is observed at zero magnetic field.

Beam radius data taken with radiochromic witness plates demonstrates the variation of radius with applied diode magnetic field (Fig. 3). In general the radius exceeds the theoretical prediction of Eq. (3). Note that the radius measurement includes some error due to coherent radial oscillations. The vertical bars in Fig. 3 indicate the approximate thickness of the beam annulus. Witness foils 4 cm beyond the anode showed well-defined annular patterns, which indicated that the outer beam particles tended to coalesce with the inner particles. The annulus thickness was always smaller at  $z = 4$  cm than at  $z = 0$ .

Energy transport data was taken with 127  $\mu\text{m}$  Ti and 25  $\mu\text{m}$  Kapton foils, which produced RMS scattering angles of  $34^\circ$  and  $4^\circ$ , respectively. In Fig. 4, energy transport within a 2.5 cm radius is plotted as a function of pressure for both a magnetized and unmagnetized beam in the  $34^\circ$  scattering situation. Transport of the magnetized beam inside  $r = 2.5$  cm is ~70% of that in the unmagnetized case for best propagation, indicating that the beam radius is minimum at ~ 30 Torr. The minimum  $r < 2.5$  cm transport corresponding to the maximum beam radius occurs at ~ 1 Torr. This is the pressure corresponding to the lowest net current, 2-4 kA. Thus, the pressure dependence of  $r < 2.5$  cm transported energy is qualitatively predicted by the radius dependence of Eq. (3). Note that for  $P = .7$  Torr, the difference between apertured calorimeter transport with and without  $B_z$  is most pronounced. This indicates that the beam annulus is almost entirely outside the aperture.



**CATHODE  $B_z$  (kG)**  
 Figure 3. Beam radius measured from radiochromic witness foils as a function of cathode magnetic field. Experimental conditions are  $P = 25 \text{ Torr}$ ,  $I_{\text{net}} = 11 \text{ kA}$ , with the plate in. Measurements were made at  $z = 10 \text{ cm}$ .

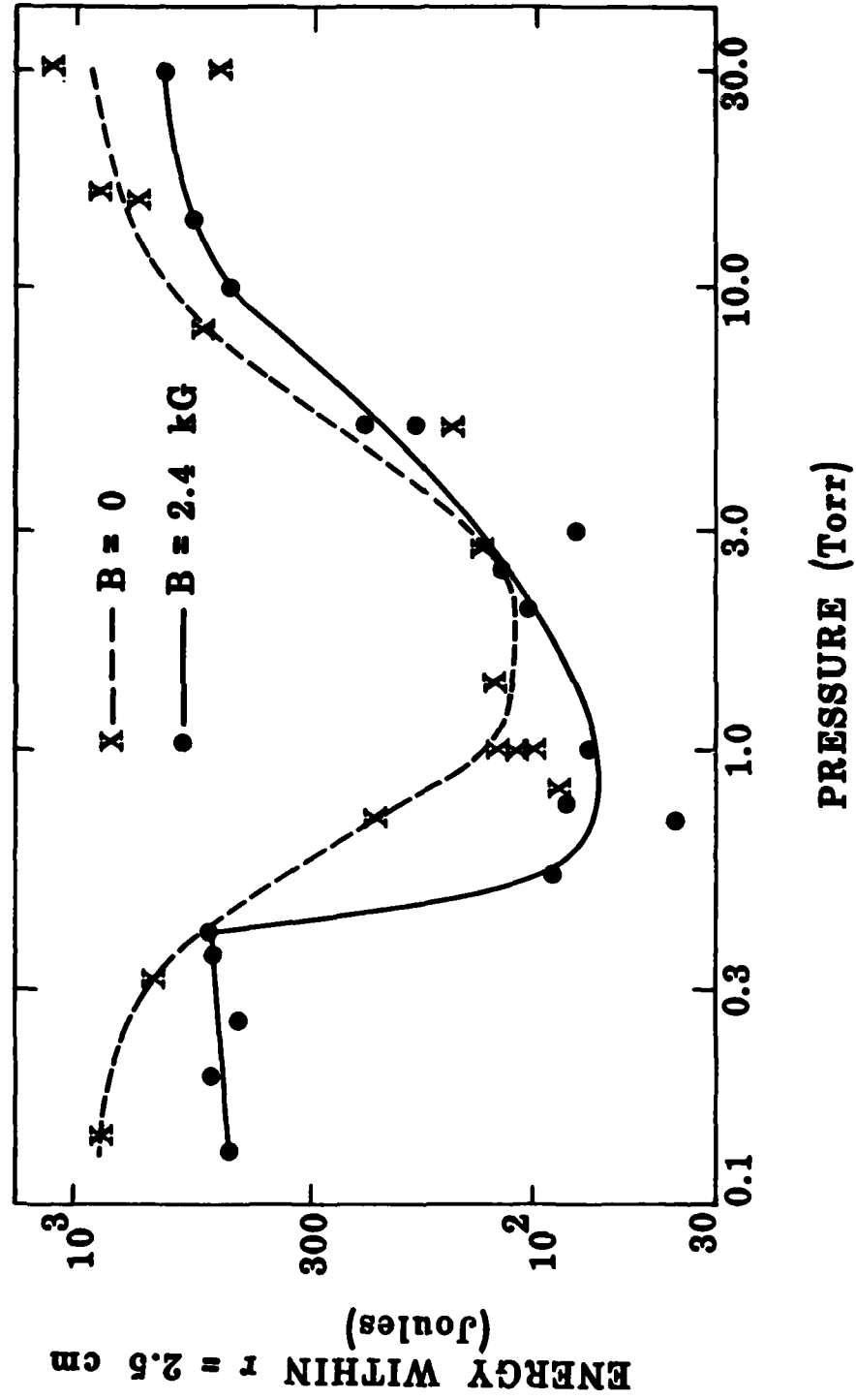


Figure 4. Energy propagation inside an  $r = 2.5$  cm aperture with and without applied diode magnetic field. Measurements were made at a 30 cm axial position.

Energy transport within  $r = 2.5$  cm differs markedly for the  $4^\circ$  scatter case shown in Fig. 5. In this case energy transport peaks at 5 Torr near the minimum net current. The dominant effects are probably the resistive hose and filamentation instability above 5 Torr, and the filamentation instability below 5 Torr. Both of these effects are expected to increase the beam diameter. The total energy transport (that is, the energy transport without the aperture) for this case is ~ 80%, independent of pressure and magnetic field, justifying interpretation of the apertured transport as being related to radius. The 20% energy loss is thought to be a combination of diode losses and high emittance particle losses.

The contrast in apertured energy propagation for the two scattering angles results from the net current dependence of Fig. 6. The current is shown for  $4^\circ$  scattering, although it is nearly independent of scattering angle. The degradation in energy propagation for the  $34^\circ$  scattering case corresponds to a low net current. This results because high radial velocity particles can only be confined and propagated when  $B_\theta$  is high. Thus, apertured energy propagation and net current dependences are similar for the  $34^\circ$  foil scattering case. For the low scattering angles, energy propagation is dominated by the effects of instabilities, and the growth rates are usually proportional to net current. Energy propagation in the rotating beam case peaks at low net currents and may be dominated by filamentation of the beam. Instability growth rates are usually reduced for beams with high temperature,<sup>5</sup> so filamentation is not expected to affect energy transport in the  $34^\circ$  scattering case. The fact that the net current is independent of cathode magnetic field (and hence, independent of beam profile) is also demonstrated by Fig. 6.

Filamentation of the hollow beam has been observed at all pressures. On the other hand beams produced from the same diode without magnetic field do not exhibit filamentation behavior. From radiochromic witness plate data, 2-5 well-defined filaments are observed for  $P < .5$  Torr. At higher

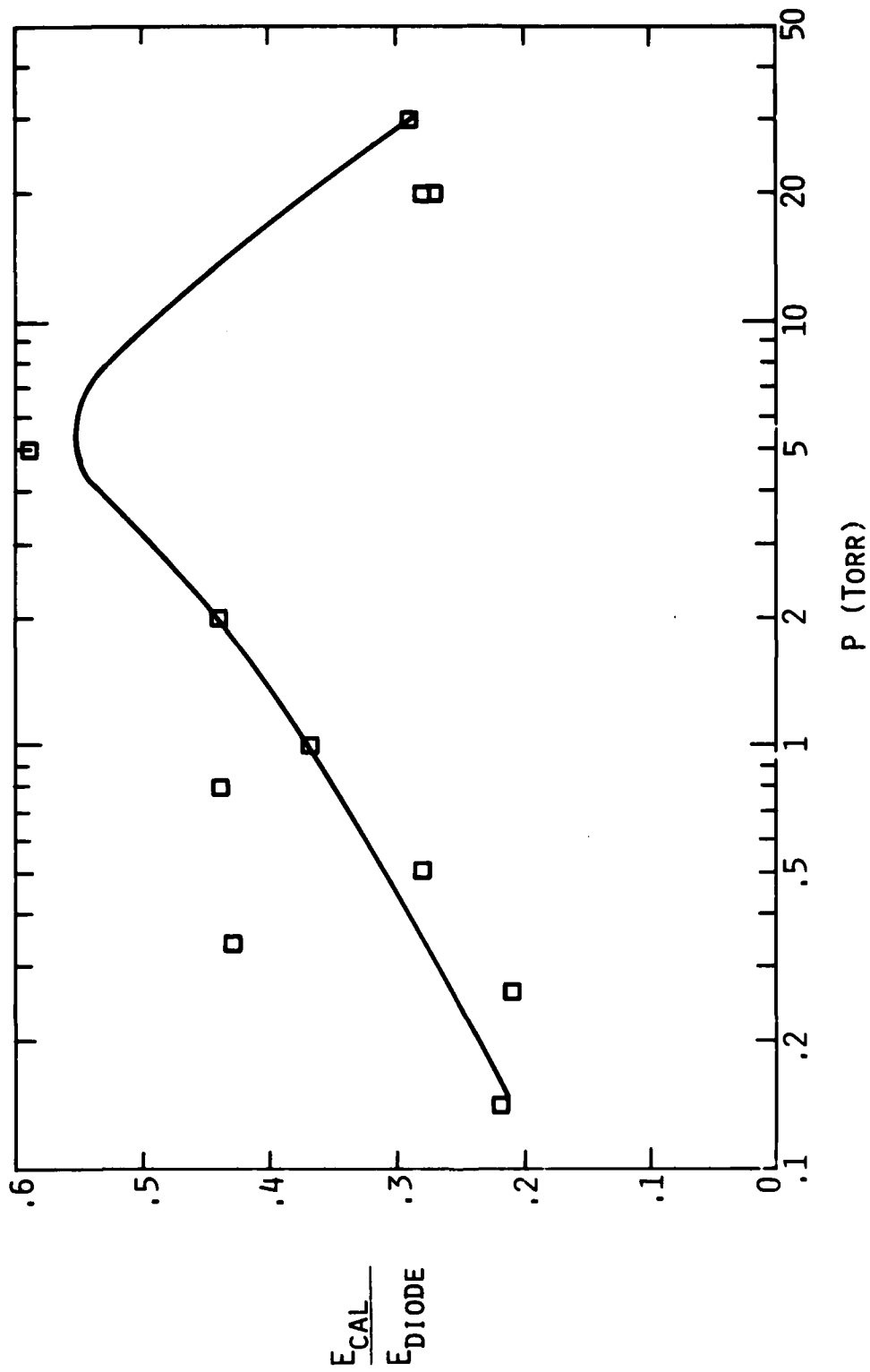


Figure 5. Ratio of injected energy ( $R < 2.5$  cm) to injected diode energy vs. pressure for 3.7 kG,  $z = 60$  cm, and a  $4^\circ$  scattering angle.

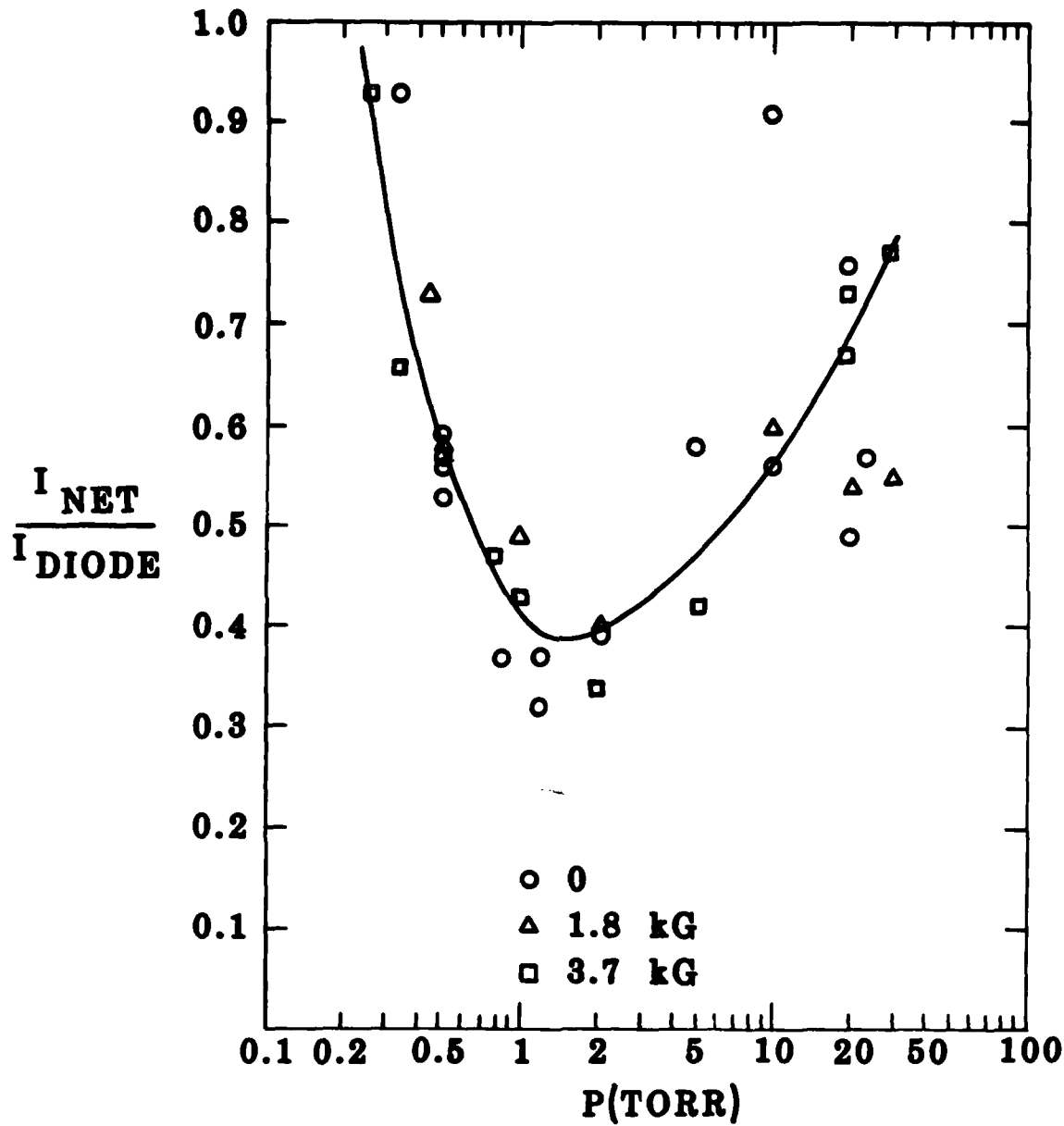


Figure 6. Ratio of net to diode current for  $4^\circ$  scattering, and a variety of cathode magnetic fields.

pressures, considerable beam distortion is observed, but the exact pattern is not as clear. Isodensity plots of two representative witness foil are shown in Fig. 7. These foils are from an axial position of 25 cm. The isodensity contours can be interpreted as being in linearly increasing order of beam current density. Note that these are contours and not an enhancement of the foil image. Inspection of Fig. 7a, for example, indicates that the highest current density lies within the '3' contour annulus with 4-5 approximately circular current enhancements. We also observe that the pattern of Fig. 7a is 'frozen' in time. Our present conjecture is that Fig. 7b represents a filamentation instability of the same type where the pattern rotates as a function of time.

Physcially, the different nature of the low and high pressure cases can be explained by interaction between the beam and return current. At low pressures, the conductivity rises rapidly about 10 nanoseconds into the pulse. The filament pattern at this time will dictate the plasma current distribution. The high plasma conductivity after this time prevents change of the spatial current density profile on a beam time scale. Thus, the beam current density is frozen in space, just as the magnetic flux is frozen. At higher pressures, diffusion of fields on a shorter time scale allows the beam pattern to vary in time and space, due to changes in beam parameters. This in turn allows the pattern to rotate as the beam rotates, thus 'smearing' the pattern.

The emittance box was used to measure beam rotation and radial and azimuthal motion away from equilibrium. The electrons transmitted through the pinholes make projections on a scintillator which reflect the transverse velocity distribution. The electron scintillations are recorded on a camera in open-shutter mode.

The average azimuthal displacement of a spot image is a measure of  $v_\theta$ , while the radial and azimuthal spot dimensions measure radial and azimuthal motion. Coherent oscillations which change phase during the



Figure 7. Isodensity contour plots showing two radiochromic foils positioned at  $z = 25$  cm. The equal transmission density contours are ranked in linear order of increasing exposure (increasing current density). (a) .3 Torr, (b) 20 Torr.



Figure 7. Concluded

pulse are denoted by elliptical spots at some arbitrary angle. The rotational velocity data is plotted as a function of radius for three magnetic fields in Fig. 8. The dashed lines indicate comparison with Eq. (1). The measured and predicted values of  $v_\theta/v_z$  are in reasonable agreement when we consider that the real equilibrium has  $\sim \pm 30\%$  shear in  $P_\theta$  while the predictions assume a single average  $P_\theta$  value.

The emittance projections are diagonals between  $30^\circ$  and  $60^\circ$  for small magnetic fields as shown in Fig. 9. This indicates that the oscillations are primarily coherent. We note that some beam filamentation precedes the emittance box measuring point. At higher magnetic fields, this diagonal structure is less well defined, probably due to radial velocities which are a function of radius due to the half-cusp transition region. Figure 9 also illustrates directly the beam rotation. The mask which precedes the scintillator is a linear array of dots while the projection is made up of two disjoint linear arrays, one on either side of the center (center is the dim dot). The fact that the two are disjoint is a result of rotation.

The absolute magnitude of radial motion varies weakly with magnetic field from  $v_r/v_z = .21$  at  $\sim 1$  kG to  $v_r/v_z \sim .27$  at 2.4 kG. From this observation we conclude that the change in equilibrium from vacuum to gas is more significant than the half cusp in causing radial oscillations in a hollow beam. Assuming the theoretical value of  $k(2\pi/\lambda)$  given by Eq. (4), the average radial particle excursion from equilibrium  $\delta a$  is  $\sim 4$  mm for  $B_C = 2.4$  kG.

Using a series of foils on a single shot, the radial oscillations were measured directly, resulting in a value of  $\sim 3$  mm for  $B_C = 3.4$  kG,  $P = .3$  Torr, and  $I \sim 12$  kA. The measured and theoretical betatron wavelengths were 12 and 11 cm, respectively.

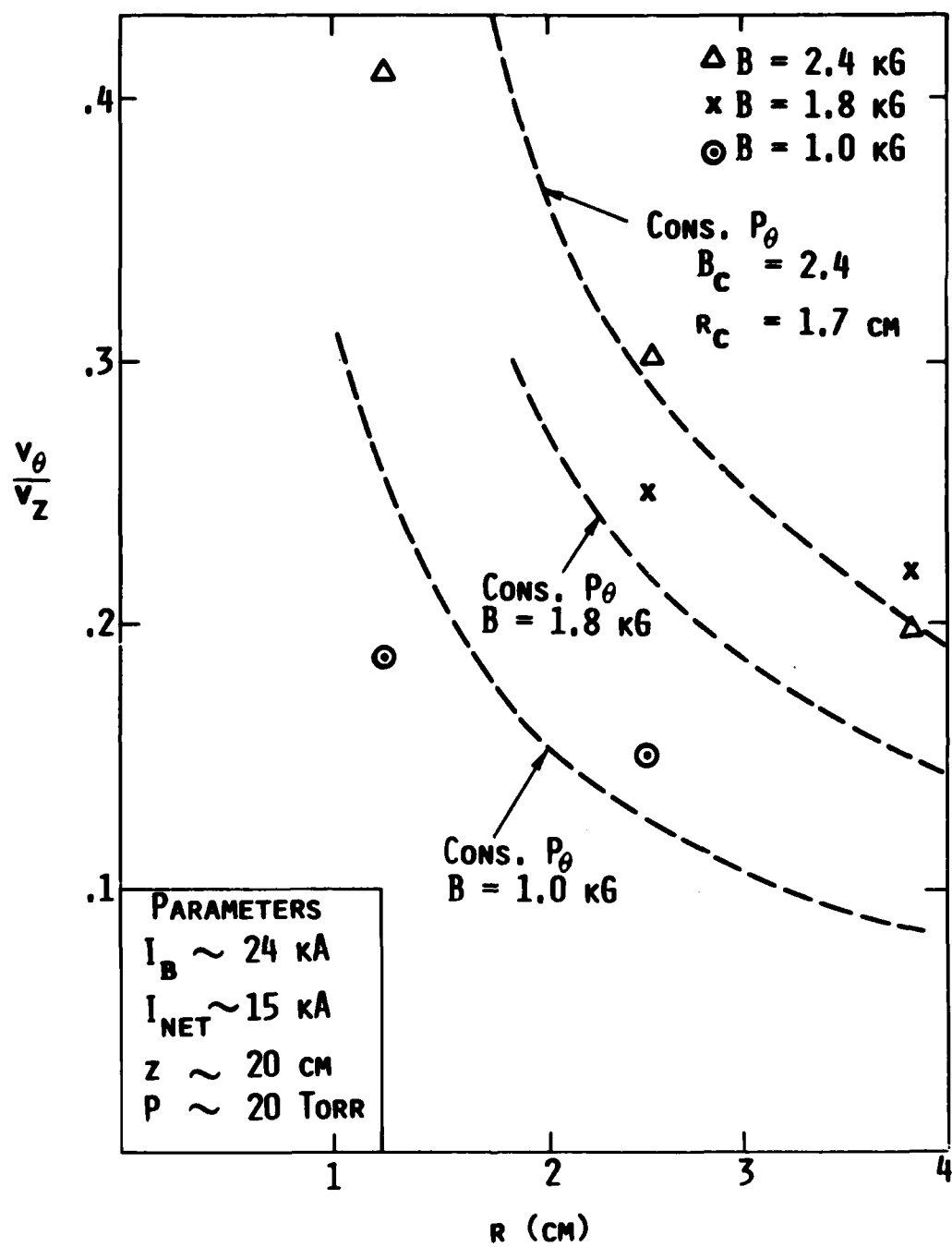
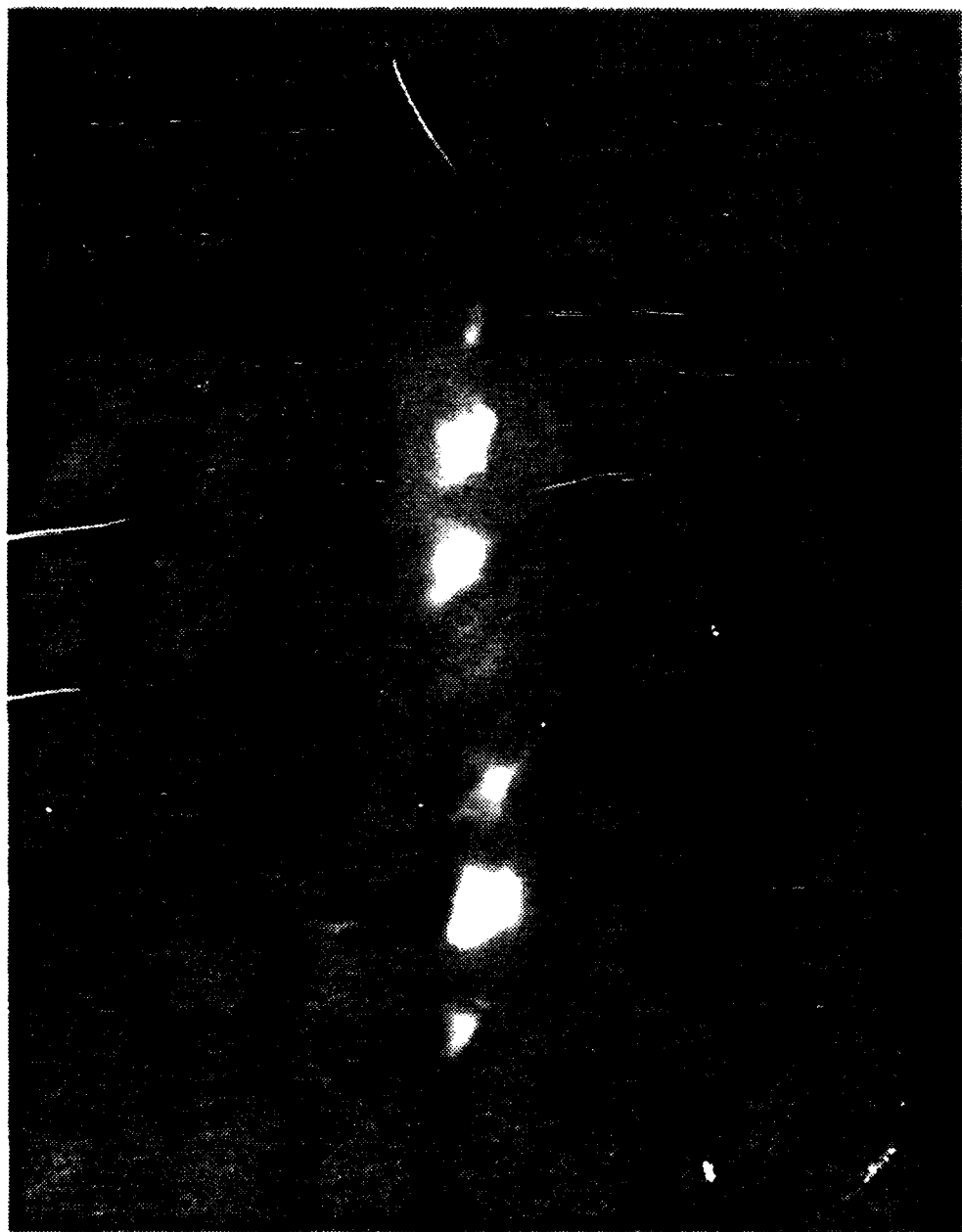


Figure 8. Beam rotation velocities as a function of radius for various cathode magnetic fields. Dashed lines are taken from Eq. (1).



**Figure 9.** Raw emittance box data illustrating the typical angled pattern for  $B_z = 1$  kG.

Measurements of beam generated axial magnetic fields were made at  $z = 18, 43$ , and  $69$  cm using axis encircling loops. These loops had to be placed in a 'cage' to prevent contributions due to  $B_\theta$  fields, electrostatic pickup, and electron bombardment. The loops had a radius of  $\sim 5$  cm.

The simplest expectation for the value of net axial fields is that the current density ratio  $J_\theta/J_z = v_\theta/v_z$ . Using this assumption, we find that the loop signal in volts is given by

$$V = \left( \frac{C_1}{\tau} \right) \mu_0 I \left( \frac{r_c^2 \omega_c}{4v_z} \right) \quad (6)$$

where  $\tau$  is the integration time constant, and  $C_1$  is a geometric factor (.6-.7 in. our case). Note that the expression above has no dependence on beam radius.

We have compared  $V$  to the Eq. (6) prediction as a function of time and find that the measured value is 20%-70% of the predicted value. Neutralization of  $\theta$  current appears to be much more complete than  $z$ -current neutralization. In general, we observe  $V \propto \omega_c$  in agreement with Eq. (6). Typical  $I$  and  $V$  signals for a variety of conditions are shown in Fig. 10. Although gross features such as rapid variations in  $B_z$  tend to follow  $I$ , the details are often markedly different.  $B_z$  also tends to fall more rapidly than  $I$  after the pulse. The late time behavior of  $B_z$  is also dependent on axial position. At  $z > 40$  cm, the  $B_z$  signal tends to drop suddenly before the end of the pulse. In general, however, we do find that  $V$  varies as diode  $B_z$  at a fixed pressure (as expected).

## DIAMAGNETIC LOOP AND NET CURRENT SIGNALS

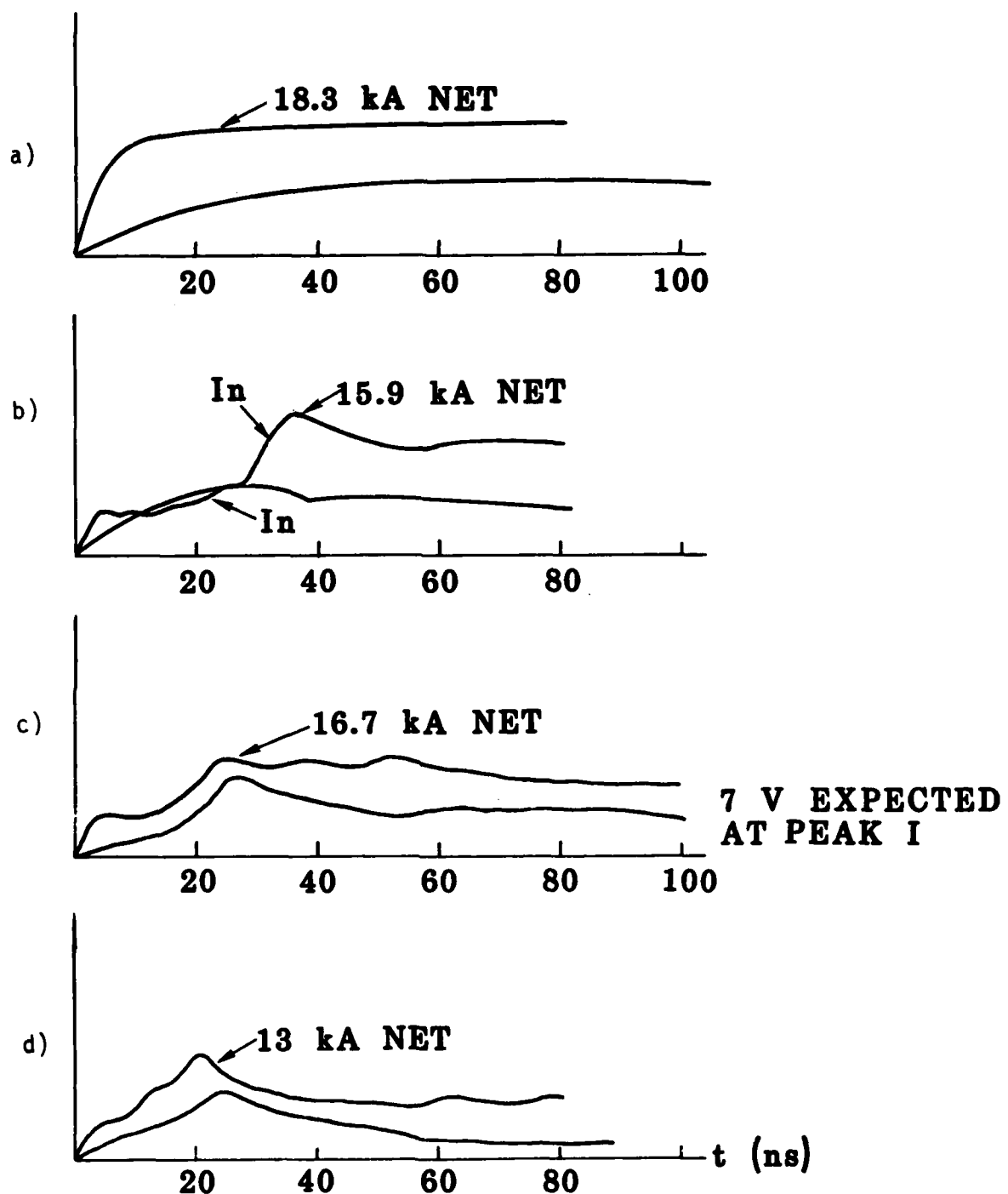


Figure 10. Comparison of  $B_z$  and  $B_\theta$  waveforms for a)  $z = 18$ ,  $P = .3$ ,  $B_z = 1.8$ ; b)  $z = 18$ ,  $P = 20$ ,  $B_z = 1.8$ ; c)  $z = 43$ ,  $P = 20$ ,  $B_z = 1.8$ ; d)  $z = 68$ ,  $P = 20$ ,  $B_z = 2.6$ . (Position  $z$  is in cm, pressure  $P$  is in torr, and diode field  $B_z$  is in kg).

There are a number of possible reasons for the difference in  $J_\theta$  and  $J_z$  characteristics. The  $J_z$  current requires a source at the metal endplate which may take a few nanoseconds to form. A closed current such as  $J_\theta$  will be immediately neutralized because it requires no source. Variations in the radial profile in  $J_\theta$  can also act to minimize  $B_z$ .

Note that over most of the measurement range (.3-20 Torr) the cyclotron frequency in the  $B_\theta$  field is comparable to the collision frequency. In this case  $\theta$  conductivity is greater than  $z$  conductivity. This effect is demonstrated graphically in Fig. 11, which shows curves of  $\omega_c = v_c$  for various plasma electron temperatures. The reduced  $B_z$  may result due to increased conductivity in  $\theta$ .

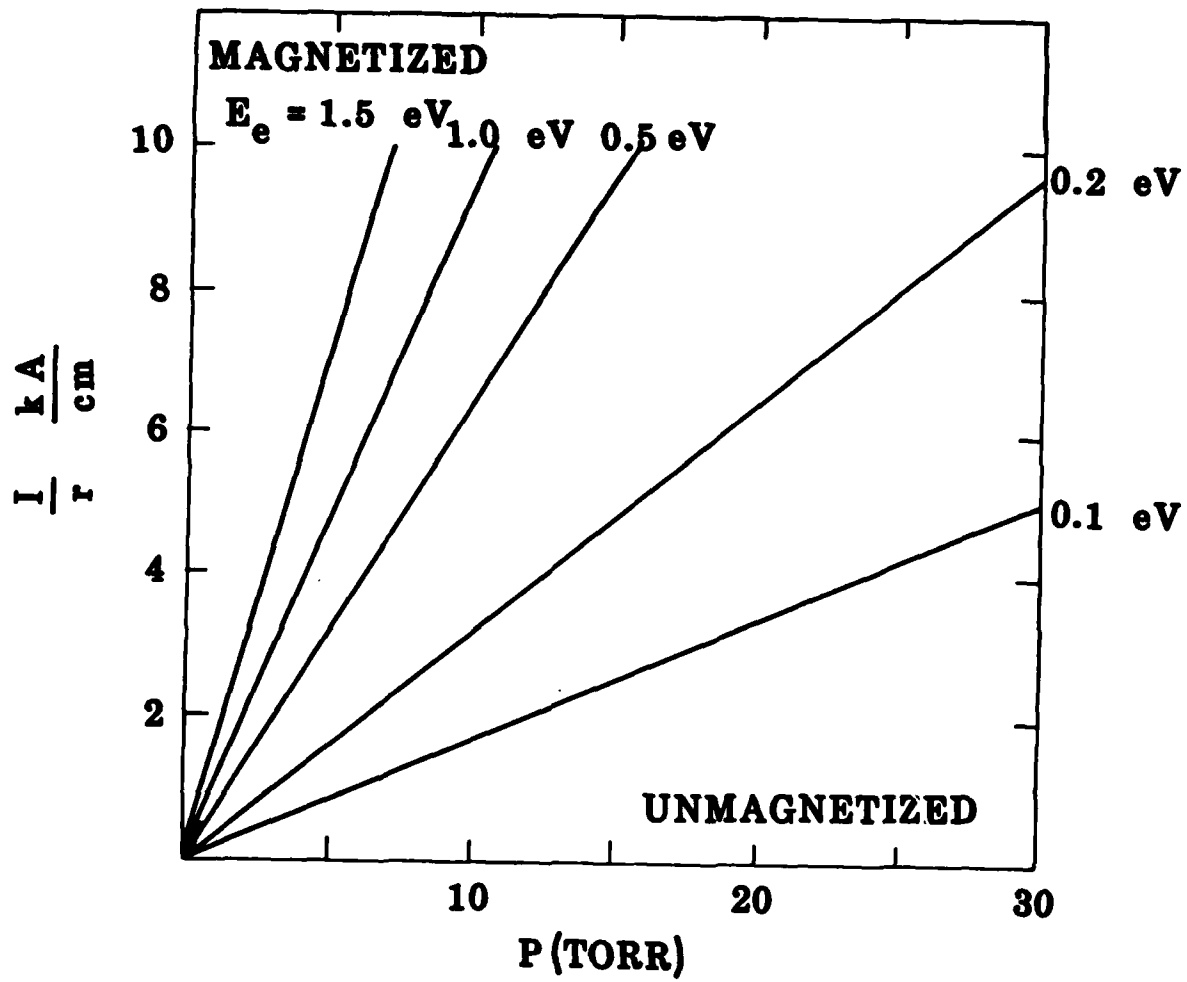


Figure 11. The plot above indicates curves of  $\omega_c = v_c$  (collision frequency) in the peak beam magnetic field where  $v_c$  is the momentum transfer collision frequency and  $\omega_c$  is the plasma electron cyclotron frequency.

## IV. NUMERICAL AND ANALYTICAL RESULTS

### A. Extraction

The two-dimensional, electromagnetic particle simulation code, CPROP,<sup>17</sup> was used to simulate extraction of the annular beam through a magnetic cusp. Azimuthal symmetry is assumed, and the coordinates of the problem are radial position and axial position ( $r, z$ ). The code treats the background gas as an Ohm's Law medium, i.e.,  $\underline{\jmath}_p = \sigma \underline{E}$ , where  $\underline{\jmath}_p$  is the conductivity and  $\underline{E}$  is the total electric field. The conductivity is computed from a model developed at Lawrence Livermore National Laboratory<sup>18</sup> and includes the effects of collisional ionization due to acceleration of secondary electrons in the electric field of the beam, and recombination of electrons with ions. The model was intended for use at somewhat higher pressures than those in the present experiment, but is expected to be approximately correct at 20 Torr, the pressure for which the simulations were done.

CPROP does not include the self-generated diamagnetic field of the beam. Experimental observations of the beam's diamagnetism tend to justify neglect of this effect as noted in Sec. III. The cusp field used in the simulations has an axial profile which agrees closely with the experimental one shown in Fig. 1(b).

Simulations were performed at three different values of the axial magnetic field as measured at the cathode tip, namely, 1 kG, 2kG, and 4 kG. The injected beam pulse had current and voltage risetimes of about 10 ns, as in the experiment. The beam was propagated in a 32 cm long, 10 cm radius pipe with perfectly conducting walls. The simulation results are shown in Fig. 12. In these figures, the beam is injected on the left into the cusp field, and starts spinning. It exits through a metal foil on the right. One might expect that the optimum condition for injection is when

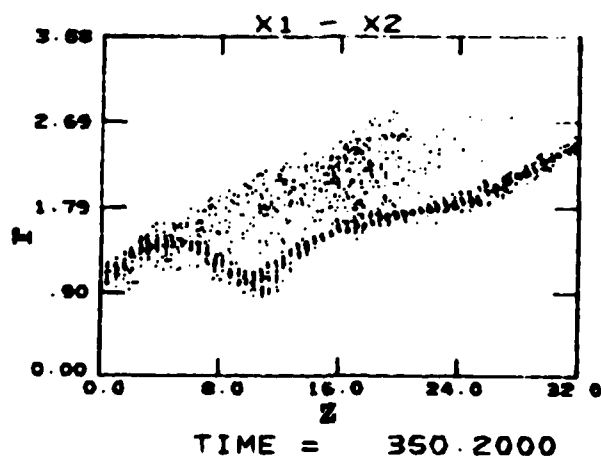
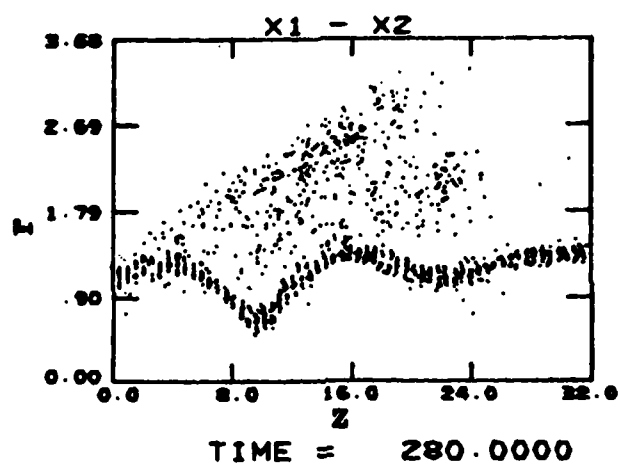
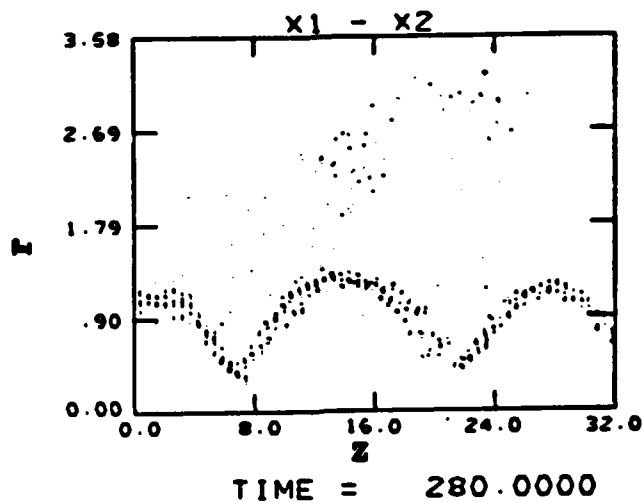


Figure 12. Simulations for  $B_z = 1$  kG, 2 kG, and 4 kG. For each value, the radial positions of the beam particles are plotted versus axial position. The radial coordinate is in logarithmic units.

the final equilibrium beam radius in the gas is approximately equal to the injection radius. This condition is satisfied for  $B_z = 2$  kG and the corresponding simulation shows the best beam behavior. At  $B_z = 1$  kG (4 kG) the equilibrium radius is about half (twice) the injection radius and the beam executes large radial bounces. The betatron wavelength is approximately 12 cm. The net current seen in the simulation was 10-20% of the beam current, which is significantly less than the 50% value measured experimentally. This is probably due to overestimation of the conductivity by the model used.

In summary, the gross features of the extraction process seen in the simulations agree with the experiment. Work is in progress on a more refined conductivity routine which will hopefully give better detailed agreement.

#### B. Filamentation

The filamentation instability clearly grows to a large value in two betatron wavelengths (see Fig. 7). A simple model of this phenomena is outlined below for the case of a hollow beam-rotation is required to set up the type of equilibrium we will study. Motion in  $r$  is constrained by angular momentum, while in equilibrium there are no  $\theta$  forces. Consider azimuthal current density perturbations of the form

$$= j n e^{i(n\theta - \beta_\theta z - k_z)} \delta(r - a) \quad (7)$$

This current density gives rise to radial magnetic fields which tend to attract particles towards the center of an enhancement. The radial magnetic field  $B$  is related to the current density by (using MKS units)

$$B_r = \frac{i \mu_0 j}{2} \quad (8)$$

We have assumed that the beam is charge, but not current neutralized. We consider only  $\theta$  forces, and the force equation is written for the perturbed  $\theta$  velocity, which we will refer to as  $\dot{\theta}$

$$ac \frac{\partial \dot{\theta}}{\partial z} = \frac{ecB}{\gamma m} = iack\dot{\theta} \quad (9)$$

From continuity we have

$$-ickj_n + in\dot{\theta}J = 0 \quad (10)$$

where  $J_\delta(r - a)$  is the current density and  $J = 1/2\pi a$ . Combining Eqs. (8)-(10) we find the spatial growth rate

$$k = \frac{i}{a} \left( \frac{nI}{2\pi I_A} \right)^{1/2} \quad (11)$$

Clearly there must exist a value of  $n$  at which growth peaks. This certainly occurs for values of  $n$  large enough that the thin beam approximation breaks down. If  $n > \pi a/\delta a$ , the  $B_r$  field is expected to be significantly less than the prediction of Eq. (8).

The derivation we present predicts that for a thin hollow beam, filamentation will occur. This effect would also occur for a rectilinear strip beam in gas, which would initially tend to become circular. Although we present no analysis on such instabilities in more conventional beam equilibria, we note that motion of particles across  $r = 0$  will probably suppress this class of instabilities in solid beams by phase mixing. The growth rate of Eq. (11) suggests that there will be  $\sqrt{2\pi n}/2$  e-foldings of the instability per betatron wavelength. For typical parameters of  $a = 2$  cm,  $\delta a = 1$  cm, ( $+ n = 6$ ) there will be approximately 6 e-foldings in 25 cm - the propagation distance of Fig. 7.

## CONCLUSIONS

We have investigated a number of properties of a new type of rotating electron beam equilibrium. The rotation is compensated by the  $B_\theta$  pinch force outside any applied axial magnetic field. Simple theoretical expectations based on force balance are reasonably correct in predicting the beam radius and rotation. Beam generated axial magnetic fields are smaller than expected. The beam is observed to filament and we suggest that this is due to the local pinch force for a thin, hollow beam. Numerical simulations of extraction are in reasonable qualitative agreement with the observations.

#### ACKNOWLEDGEMENTS

The authors would like to thank B. B. Godfrey, R. B. Miller, M. C. Clark, and M. Mazarakis for useful discussions during the course of this work. We also thank T. Montoya and R. L. Copeland for their technical assistance during the performance of the experiments.

This work was supported by Sandia National Laboratories, Pulsed Power Directorate and by the Air Force Weapons Laboratory, High Energy Physics Division.

## REFERENCES

1. S. Graybill, IEEE Trans. Nuc. Sci. NS-18, 438 (1971).
2. R. J. Briggs, et. al., Proceedings 2nd International Conference on High Power Electron Beam Research and Technology (Cornell University, Ithaca, NY, 1977), Vol. I, p. 319.
3. D. A. Hammer and N. Rostoker, Phys. Fluids 13, 1831 (1970).
4. J. A. Nation and W. L. Gardner, Nuc. Fusion 11, 5 (1971).
5. E. P. Lee, Phys. Fluids 21, 1327 (1978).
6. M. L. Andrews, et. al., Phys. Rev. Lett. 27, 1428 (1971).
7. C. A. Kapetanakos, W. M. Black, and C. D. Striffler, Appl. Phys. Lett. 26, 368 (1975).
8. J. D. Sethian, et. al., Phys. Fluids 21, 1227 (1978).
9. J. D. Sethian, et. al., Phys. Fluids 23, 1880 (1980).
10. S. Yoshikawa, Phys. Rev. Lett. 26, 295 (1971).
11. V. K. Neil "Quadrupole vs. Solenoidal Focusing to Suppress the Image Displacement Instability in Linear Induction Accelerators," UCID-17838, Lawrence Livermore National Laboratory, 1978.
12. R. J. Adler, Part. Accel. 12, 39 (1982).
13. C. A. Kapetanakos, P. Sprangle, and S. J. Marsh, Phys. Rev. Lett. 49, 741 (1982).
14. J. W. Poukey, private communication.
15. P. Gehringer, et. al., Int. J. Appl. Rad. Isot. 33, 27 (1982).
16. A. G. Englehardt, A. V. Phelps, and C. G. Risk, Phys. Rev. 135, A1566 (1964).
17. B. B. Godfrey, AMRC-R-367, Mission Research Corporation, Albuquerque, (1982).
18. See e.g., F. W. Chambers, UCID-18302, Lawrence Livermore National Laboratory (1979).

